3D-printed auxetic design delivers breakthrough in sensitive and wearable tactile sensors

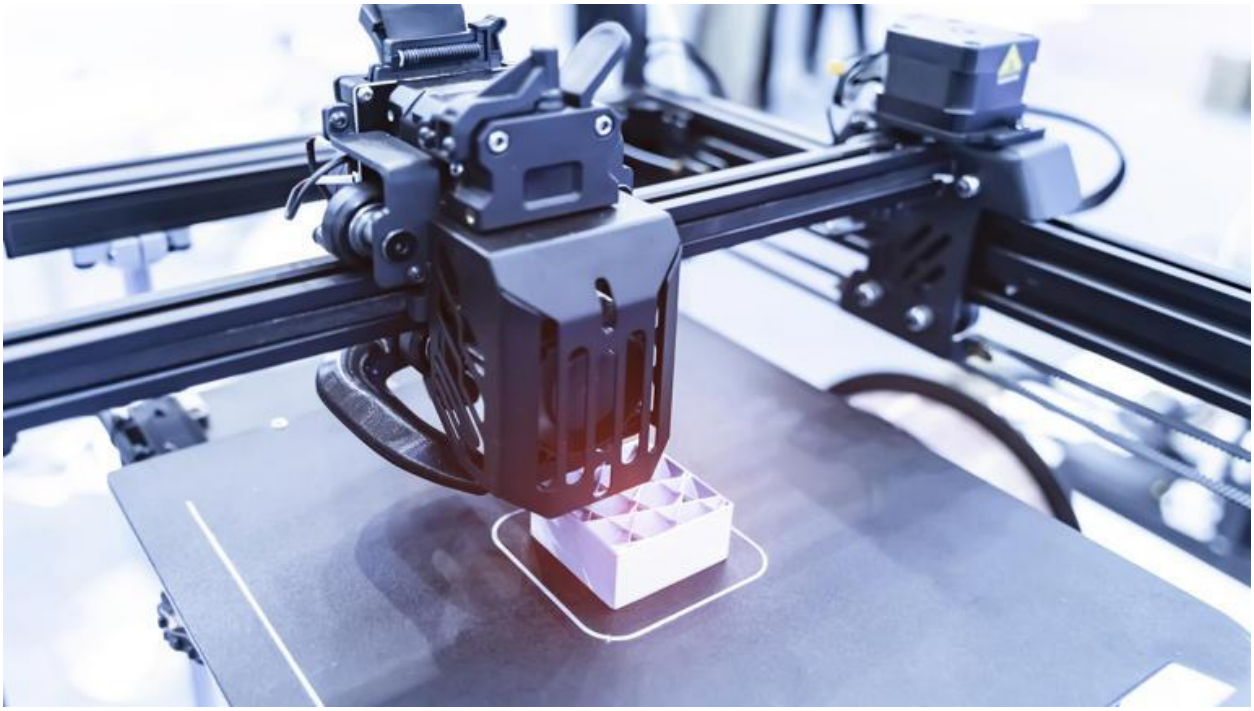

3D-printed auxetic design delivers breakthrough in sensitive and wearable tactile sensors

Tactile sensors have become essential in robotics, prosthetics, wearable devices, and healthcare monitoring.

By detecting and converting pressure or force into electrical signals, these devices allow machines and medical tools to respond more accurately to the environment.

For years, researchers have worked to expand the sensing range and boost sensitivity. One promising route has been mechanical metamaterials, which exhibit unique properties not found in conventional materials.

Among them, auxetic mechanical metamaterials (AMMs) stand out. They feature a negative Poisson's ratio, which enables inward contraction and localized strain concentration when compressed, a counterintuitive trait that makes them highly attractive for advanced sensing applications.

Despite their potential, AMMs have faced practical obstacles. Existing technologies struggle with fabrication challenges and integration issues that prevent large-scale adoption in real-world systems.

Strain, sensitivity, and stability

A research team from the Seoul National University of Science and Technology has now taken a major step forward. Led by Mingyu Kang and Dr. Soonjae Pyo, the group developed a novel 3D AMM-based tactile sensing platform.

Their findings demonstrate how a cubic lattice with spherical voids, fabricated using digital light processing (DLP)-based 3D printing, can unlock new design possibilities.

The team tested their 3D-printed auxetic metamaterials in both capacitive and piezoresistive sensing modes. In the first, pressure alters electrode spacing and dielectric distribution. In the second, a carbon nanotube coating changes resistance under load.

Kang explained that the unique negative Poisson's ratio behavior enables inward contraction under compression, which concentrates strain in the sensing region and boosts sensitivity.

"The auxetic design strengthens sensor performance in three ways—enhancing sensitivity through localized strain concentration, maintaining stability in confined structures, and minimizing crosstalk between sensing units," he said.

He added that, unlike conventional porous structures, the design avoids lateral expansion, making it more wearable and less prone to interference. "With digital light processing-based 3D printing, we can precisely program structural performance and customize geometry without changing the base material," Mr. Kang noted.

The team validated the concept with two demonstrations: a tactile array for spatial pressure mapping and object classification, and a wearable insole system capable of monitoring gait patterns and detecting pronation types.

Smart insoles and beyond

According to Dr. Pyo, the proposed sensor platform can be applied across diverse fields, from smart insoles for gait monitoring to robotic hands for precise object manipulation and wearable systems that track health comfortably without disrupting daily activities.

"The auxetic structure preserves its sensitivity and stability even when confined within rigid housings, such as insole layers, where conventional porous lattices typically lose performance," he said.

He further noted that the design's scalability and compatibility with multiple transduction modes make it "suitable for pressure mapping surfaces, rehabilitation devices, and human-robot interaction interfaces that require high sensitivity and mechanical robustness."

Looking ahead, these auxetic-structured 3D-printed tactile sensors could reshape wearable electronics. They offer the promise of continuous, high-fidelity monitoring of human movement, posture, and health metrics.

Their adaptability and independence from specific materials also open doors to personalized sensors for prosthetics, medical applications, and immersive haptic systems.

As additive manufacturing technology becomes more widespread, the researchers believe customizable tactile interfaces may soon become standard across consumer products, healthcare devices, and robotics, paving the way for the next generation of smart, responsive systems.

The findings have been published in *Advanced Functional Materials*.

Additively Manufactured 3D Auxetic Metamaterials for Structurally Guided Capacitive and Resistive Tactile Sensing

Mingyu Kang, Hong-Gap Choi, Keun Park, Soonjae Pyo
First published: 06 July 2025 **https://doi.org/10.1002/adfm.202509704**

Abstract

Auxetic mechanical metamaterials (AMMs) with negative Poisson's ratio behavior offer an effective strategy for improving tactile sensor performance by enabling inward contraction and localized strain concentration under compression. This study presents a 3D AMM-based tactile sensing platform based on a cubic lattice with spherical voids, fabricated via digital light processing. The structure exhibits auxetic deformation under compressive loading, with inward collapse of ligaments confirmed through simulations and experimental analyses. Two sensor configurations are implemented, namely, a capacitive sensor that responds to pressure by modulating electrode spacing and dielectric distribution, and a resistive sensor based on a

conformally coated network of carbon nanotubes that alters resistance under load. Electromechanical measurements confirm enhanced sensitivity compared to sensors based on conventional porous geometries with positive Poisson's ratio. The platform also maintains reliable operation over repeated cyclic loading. Its practical functionality is demonstrated through two representative applications—a 4 × 4 tactile array for spatial pressure mapping and object classification and a wearable insole system capable of monitoring gait patterns and detecting pronation types. The study findings validate the potential of architected auxetic structures as a scalable and versatile foundation for next-generation tactile sensing platforms.

1 Introduction

Tactile sensors detect and convert physical stimuli such as pressure, force, and deformation into electrical signals, enabling artificial systems to interact effectively with their environments. Owing to the growing demand for tactile sensors in fields, including robotics,[1, 2] prosthetics,[3, 4] healthcare monitoring,[5, 6] and wearable electronics,[7, 8] extensive efforts have been made to enhance sensor performance through both material innovation and structural engineering.[9, 10] As regards the materials aspect, conductive nanocomposites and soft elastomeric polymers have been widely employed to improve signal responsiveness and mechanical durability.[11] By embedding nanomaterials such as carbon nanotubes (CNTs), graphene, and metallic nanowires into flexible matrices, sensors can form dense percolation networks that improve conductivity and sensitivity while maintaining mechanical compliance. In parallel, structural engineering approaches have been introduced to amplify pressure-induced responses.[12] Microstructured surfaces composed of domes, pyramids, or ridges concentrate stress at contact points, generating larger electrical outputs under light loads. Internally porous frameworks, resembling foams or sponges, increase compressibility and local strain concentration, thereby broadening the sensing range and enhancing sensitivity. These advances in material composition and structural architecture have collectively enabled the development of tactile sensors capable of detecting subtle mechanical cues with high fidelity and robustness.

Mechanical metamaterials (MMs) have emerged as a powerful approach for tailoring the mechanical behavior of sensors and actuators.[13-15] In contrast to conventional materials whose properties are governed primarily by intrinsic composition, MMs derive their functionality from periodic cellular architectures. MMs can be programmed to exhibit a range of unconventional behaviors, such as tunable stiffness,[16] zero Poisson's ratio,[17] negative Poisson's ratio (NPR),[18] and anisotropic deformation[19] through deliberate engineering of unit-cell topology and global lattice configuration. These characteristics are not only mechanically novel but also highly customizable, enabling the modulation of deformation pathways and stress distributions according to application-specific requirements. This versatility is particularly beneficial in soft robotics, haptic interfaces, and wearable electronics, wherein compliance, directional response, and integration flexibility are critical. In sensing platforms, MMs can be designed to focus mechanical strain into specific regions, amplifying the response of embedded functional materials.[20] In actuators, they provide a means of translating modest input forces into magnified or directional outputs through geometrically programmed motions.[21]

Among the diverse MM architectures, auxetic mechanical metamaterials (AMMs) stand out because of their unique NPR behavior.[22-24] Unlike typical materials that expand laterally when compressed, AMMs contract inward. This counterintuitive behavior offers several mechanical advantages, including enhanced energy dissipation, increased deformability, and improved fracture resistance. Owing to their unique mechanical properties, AMMs have recently been explored as functional platforms for sensing devices, including strain[25-27] and pressure sensors.[28-33] When incorporated into piezoresistive configurations, AMMs enhance the sensing performance by facilitating strain localization and increasing the formation of conductive pathways upon deformation. For example, Huang et al. reported flexible strain sensors based on auxetic metamaterials, capable of wide-range bidirectional strain sensing and real-time detection of unstable robotic grasping through an arrayed sensing system and simplified signal processing.[32] Shi et al. also developed a piezoresistive sensor based on a hyperbolic auxetic microstructure and reported significantly improved sensitivity compared to conventional porous materials with positive Poisson's ratios (PPRs).[30] Their freeze-dried auxetic structure promoted inward contraction under compression, which increased the number of contact points and conductive channels, thereby reducing the resistance and improving the signal responsiveness across a wide pressure range. In addition, a recent study proposed an AMM-assisted triboelectric nanogenerator, wherein a precompressed NPR polyurethane scaffold was combined with a positively expanding collagen aggregate foam core.[31] This hybrid design facilitated a synergistic deformation between the auxetic shell and conventional friction layer, significantly enhancing the contact area and mechanical energy absorption under compression. Despite their promising functionality, these approaches rely on complex template-based fabrication processes, such as directional freeze-drying and mold-assisted casting. These techniques often impose constraints on geometric tunability, scalability, and production throughput, limiting their applicability or integration into diverse tactile systems. Recent studies have explored additive manufacturing to fabricate AMM structures for sensing applications. While these strategies effectively leverage additive manufacturing to overcome the limitations of template-based fabrication, most reported designs remain confined to 2D[34] or quasi 3D[35] architectures, restricting the realization of volumetric auxetic deformation. Furthermore, the sensing mechanisms have primarily focused on piezoresistive responses, leaving other transduction modes underexplored.

To address the aforementioned fabrication and integration challenges, we propose an additively manufactured tactile sensing platform that employs a 3D-architected AMM framework. Unlike mold- or template-based methods, our approach allows for flexible design and straightforward customization of mechanically functional architectures. Notably, the proposed AMM features a geometrically simple configuration, consisting of a cubic lattice with a central spherical void, which facilitates predictable mechanical behavior and efficient manufacturability. We present two tactile sensor configurations based on this platform—a capacitive sensor, wherein the AMM serves as a deformable dielectric layer whose compression alters both the electrode spacing and effective permittivity (ε_{eff}); and a resistive sensor, wherein the AMM is coated with conductive CNTs to form a percolative network that responds to pressure through resistance changes. Structural and electromechanical characterizations confirmed that the AMM-based sensors exhibit improved sensitivity compared to conventional porous structures with a PPR. Interestingly, although AMMs have primarily been explored in

piezoresistive sensing configurations, this study uniquely extends their utility to capacitive tactile sensors. Finally, we demonstrate the practical utility of the AMM-enabled sensors through two representative applications—a 4 × 4 sensor array for spatial pressure mapping and object classification, and a smart insole system for real-time gait monitoring and pronation analysis. The results highlight the potential of 3D-printed AMMs as a scalable and versatile platform for next-generation tactile sensing technologies.

2 Results and Discussion

2.1 Concept and Design

Figure 1 presents the overall concept of the proposed AMM-based tactile sensor. The AMM is designed as a 3D porous structure with periodically arranged unit cells, and the fabrication employs digital light processing (DLP)-based additive manufacturing with soft, elastomeric photopolymer resins (Figure **1a**). A key characteristic of the structure is its auxetic behavior, which enables inward contraction under compressive loading. The resulting NPR effect enhances local strain concentration, significantly improving the sensitivity of tactile sensors. To exploit this unique mechanical response for tactile sensing, two sensing mechanisms—capacitive and resistive—were integrated into the AMM structure (Figure **1a**, right). In the capacitive configuration, the AMM is sandwiched between copper film electrodes, and pressure-induced deformation alters the electrode spacing, leading to a measurable capacitance change. In the resistive configuration, a CNT-coated AMM (C-AMM) serves as the sensing layer, wherein compression increases the number of conductive pathways, thus reducing electrical resistance.

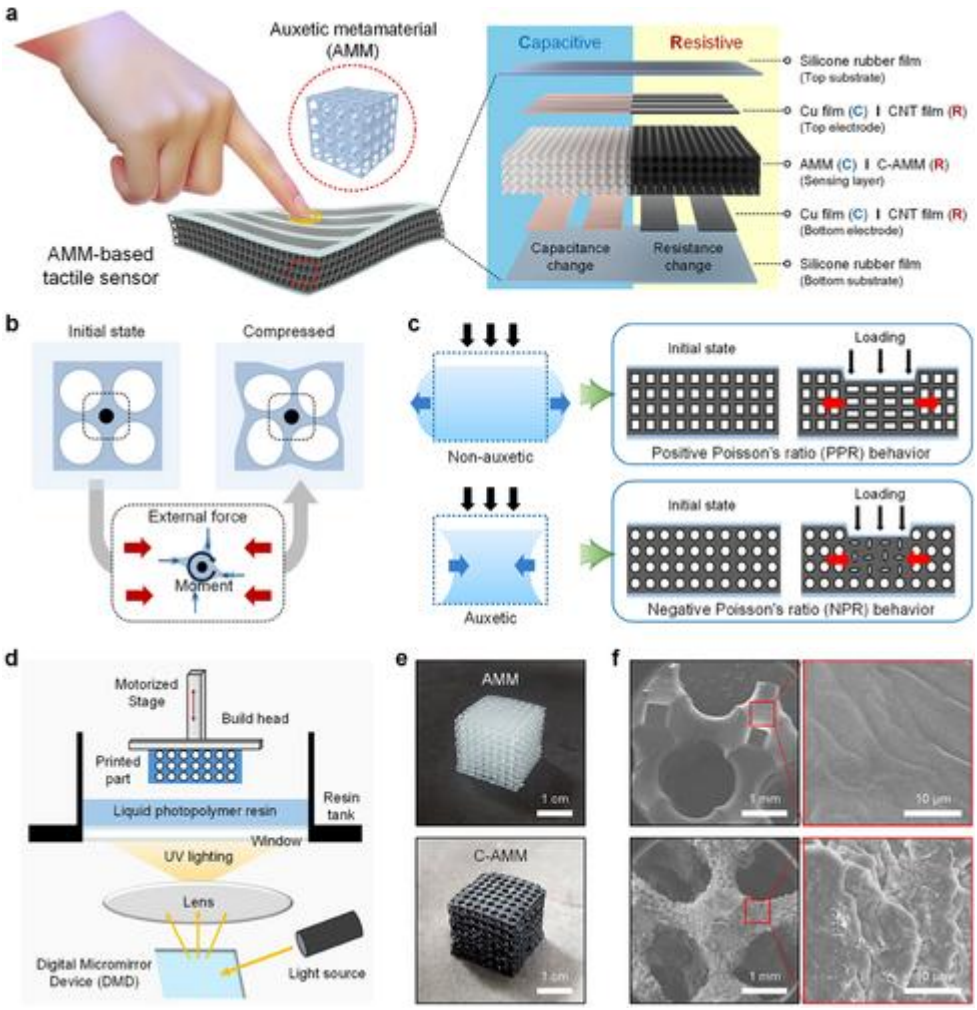

Figure 1

Open in figure viewerPowerPoint

Concept and design of AMM-based tactile sensor. a) Schematic of AMM-based tactile sensor, in which AMMs serve as the core sensing structure. The sensor enables both capacitive and resistive sensing modes via structural integration. b) Structural mechanism of the AMM unit cell under compression. The buckling and rotational deformation of ligaments surrounding spherical voids induce inward contraction and NPR behavior. c) Comparison of deformation behavior between conventional non-auxetic (PPR) and auxetic (NPR) porous materials under localized compression. AMM concentrates strain at the contact site, whereas non-auxetic structures disperse it laterally. d) Schematic of DLP-based additive manufacturing process used to fabricate the AMM with high geometric fidelity. e) Optical images of fabricated AMM and C-AMM. f) SEM images of AMM and C-AMM. CNTs form a conformal conductive layer on the ligament surfaces, forming a continuous sensing network.

Figure **1b** illustrates the structural mechanism underlying the auxetic behavior of the proposed AMM. Each unit cell consists of a cubic framework with one centrally positioned spherical void and six hemispherical voids removed from the center of each face, resulting in a fully interconnected 3D porous lattice when tessellated (Figure **S1**, Supporting Information). When the AMM is subjected to uniform compressive loading, the thin ligaments surrounding the

spherical voids undergo buckling and rotational deformation, which leads to a coordinated inward collapse as opposed to lateral expansion.[36] The auxetic response arises from two primary mechanisms. First, buckling-induced contraction occurs as the ligaments fold inward under compressive stress, effectively reducing the lateral dimensions of the structure. Second, rotational kinematics of adjacent unit cells further amplify this effect, ensuring that the deformation propagates uniformly throughout the structure. Figure **1c** illustrates the localized deformation behavior of the AMM under compressive loading, contrasting it with that of conventional porous structures. In non-auxetic materials, a localized force causes individual pores to collapse in a manner that laterally expands the structure, resulting in a PPR. This outward expansion disperses the strain, reducing the deformation concentration at the point of applied pressure. AMM behaves differently, as it undergoes inward contraction under localized compression, resulting in NPR behavior. When a force is applied to specific regions, the surrounding ligaments bend inward, triggering a chain reaction in which adjacent unit cells rotate and contract in a synchronized manner. Instead of dispersing the strain outward, the AMM effectively redirects the compressive stress into its structural framework, ensuring that the deformation remains concentrated at the point of contact. The localized auxetic response enhances the ability of the AMM to detect and respond to applied forces with high sensitivity, making it well-suited for tactile sensing applications.

The fabrication of the AMM was achieved using DLP-based additive manufacturing, which is a high-resolution 3D printing technique capable of producing complex micro-architected structures with precision (Figure **1d**).[37] In this process, a digital micromirror device selectively projects patterned UV light onto a liquid photopolymer resin, curing the exposed regions layer by layer to form the desired geometry. The layer-by-layer solidification allows for the fabrication of intricate porous structures while maintaining fine structural details; this is essential for preserving the designed auxetic behavior. DLP was selected over the other 3D printing techniques owing to its ability to produce continuous, defect-free struts with well-defined geometries. Unlike fused deposition modeling, which suffers from stair-step effects and layer adhesion issues, or direct ink writing, which relies on extrusion-based deposition with limited resolution, DLP enables the fabrication of seamless and highly interconnected porous networks. The photographs of the fabricated AMM and C-AMM are shown in Figure **1e**. The AMM, printed using an insulating photopolymer resin, was modified by applying a thin CNT layer via spray coating to introduce electrical conductivity. The CNT coating formed a conductive network on the surface, enabling the structure to function as a piezoresistive sensing material. To confirm the successful fabrication of the AMM and uniform deposition of CNTs, the surfaces of the AMM and C-AMM were examined using scanning electron microscopy (SEM). As shown in Figure **1f**, the AMM has a uniform and interconnected porous structure. After spray coating, CNTs form a conformal conductive layer along the ligaments and create a continuous network.

2.2 Deformation Analysis and Structural Characteristics

The mechanical behavior of the AMM is directly influenced by its structural design, particularly its auxetic characteristics and porosity. To examine its deformation behavior under compressive loading, finite element method (FEM) simulations were performed. A 2D model

was first adopted to capture the characteristic buckling-induced auxetic response. Upon vertical loading, the simulated structure exhibited lateral contraction due to pore buckling, demonstrating an NPR response (**Figure 2a**). We also performed a 3D FEM simulation using a 1/8 symmetric domain of the AMM structure (see Figure **S2**, Supporting Information, for the detailed FEA process). The 3D simulation confirmed the characteristic pore buckling and auxetic contraction under compressive strain, consistent with the 2D model. Building on the simulation results, mechanical tests were conducted to evaluate the structural properties of the fabricated specimens. To investigate the effect of porosity, the diameter of the spherical void within each unit cell was varied (Figure **S3**, Supporting Information). The unit cell was designed as a 2 mm cubic framework, with the porosity controlled by adjusting the void diameter (*d*).
Figure **2b** illustrates the relationship between *d* and overall porosity. Increasing *d* from 1.55 to 1.65 mm led to an increase in porosity from 71.9% to 78.6%, demonstrating the direct influence of geometric modifications on structural density. The effect of porosity on compressibility was further examined through compression experiments (Figure **2c**). The stress–strain curves revealed that higher-porosity structures experienced greater compressive deformation under the same applied stress, whereas lower-porosity structures exhibited higher stiffness and resisted deformation more effectively. This confirmed that increasing porosity enhanced compressibility, allowing for the structure to deform more easily under external pressure. To explore the relationship between porosity and auxetic behavior, the Poisson's ratios of the specimens were measured under compressive loading (Figure **2d**). At small strains, all structures initially exhibited PPR behavior, similar to conventional porous materials. However, as compression progressed, Poisson's ratio rapidly decreased, shifting into the NPR regime. The minimum Poisson's ratio was observed at ≈10–15% strain, followed by a gradual recovery at higher deformations. This behavior originates from the buckling-induced deformation mechanism of the AMM. At low strains, the ligaments remain mostly undeformed, with elastic bending causing an initial increase in Poisson's ratio. As the strain increases, buckling and rotational deformation dominate, leading to inward contraction and a sharp decrease in Poisson's ratio. This auxetic response enables the AMM to exhibit lateral contraction under compression, rather than expansion. At higher strains, structural densification further limits ligament rotation, causing the Poisson's ratio to gradually increase again. This effect is more pronounced in lower-porosity structures, wherein higher stiffness restricts deformation, leading to faster Poisson's ratio recovery. In contrast, higher-porosity structures sustain lower Poisson's ratios over a wider strain range, demonstrating that greater porosity enhances auxetic performance. Given that the 78.6% porosity structure exhibits the most favorable combination of auxetic response and compressibility, it was selected for subsequent experiments to optimize the AMM-based tactile sensor. It should be noted that we attempted to fabricate AMM structures with even greater porosity by increasing *d*. However, when the *d* exceeded 1.65 mm, the printed structures became too fragile and collapsed during the DLP printing process. Conversely, when the porosity was reduced by decreasing *d* to 1.5 mm, the resulting structures had overly thick ligaments that inhibited symmetric buckling (Figure **S4**, Supporting Information). Instead of exhibiting inward contraction, the structure deformed asymmetrically through lateral bending. To further substantiate the auxetic behavior, we compared the strain-dependent Poisson's ratio of the AMM structure obtained from experiments and FEM simulations (Figure **S5**, Supporting Information). Although the 3D FEM analysis was constrained to 9.4% compressive strain due to an element distortion instability in

the self-contact region, the results exhibited a consistent trend with the experimental measurements, including the transition from PPR to NPR. Notably, when the simulated curve was shifted by ≈1.8% strain to the left, it closely overlapped with the experimental data. This offset likely originates from residual pre-strain introduced during the post-curing processes of the DLP-printed structures.

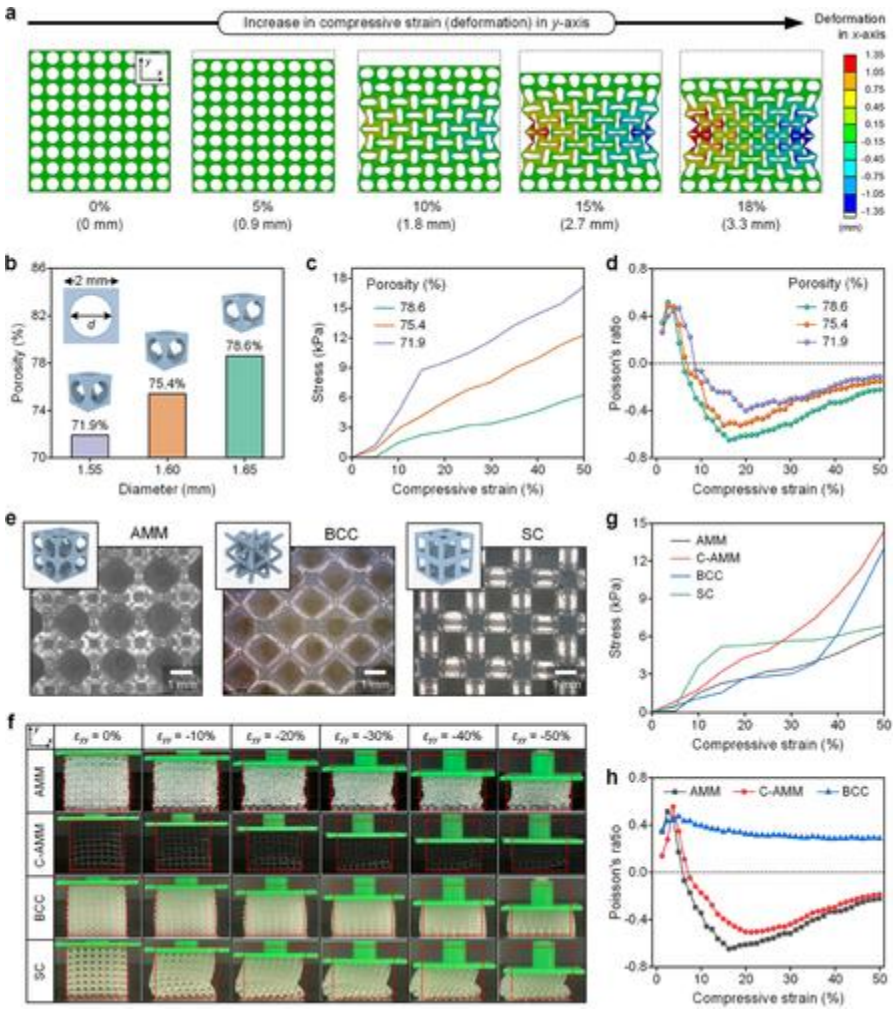

Figure 2

Open in figure viewerPowerPoint

Deformation behavior and mechanical characteristics of AMM and control lattice structures. a) 2D FEM simulation of AMM under increasing compressive strain, showing inward contraction and NPR behavior. b) Porosity variation of AMM as a function of spherical void diameter within the unit cell. c) Compressive stress–strain curves for AMMs with different porosities. Higher porosity leads to increased deformability. d) Strain-dependent Poisson's ratio for AMMs with different porosities. NPR behavior is most pronounced in the highest-porosity structure. e) Optical microscopy images and unit cell schematics of AMM, BCC, and SC structures fabricated via DLP 3D printing. f) Photographs of four structures under increasing compressive strain, showing inward contraction for auxetic AMMs and lateral expansion or instability for conventional lattices. g) Compressive stress–strain curves of four structures. C-AMM exhibits the highest stiffness owing to the CNT coating. BCC shows densification at high strains, while SC

plateaus owing to structural instability. h) Poisson's ratio profiles of AMM, C-AMM, and BCC under compression. AMM and C-AMM enter the NPR regime at ≈10%–15% strain, while BCC maintains a PPR throughout.

To evaluate the mechanical performance of the AMM, a comparative analysis was conducted against two conventional lattice structures: body-centered cubic (BCC) and simple cubic (SC). The BCC structure consists of intersecting diagonal struts, forming a highly interconnected network, while the SC structure comprises orthogonally arranged beams, resulting in a more rigid configuration. Figure **2e** presents the unit cell designs of the three structures alongside optical microscope images of the DLP 3D-printed specimens. Each structure was fabricated with identical porosity, ensuring that differences in mechanical behavior were attributed solely to lattice geometry rather than material density (Figure **S6**, Supporting Information). The deformation behavior of the four lattice structures under compressive strain is shown in Figure **2f**. AMM and C-AMM exhibit auxetic behavior; they show lateral contraction when subjected to vertical compression, confirming their NPR effect. The microscale deformation of C-AMM was further examined using SEM (Movie **S1** and Figure **S7**, Supporting Information). The SEM images revealed the progressive inward collapse of the unit cell ligaments, providing direct evidence of the buckling-driven auxetic response depicted in Figure **1b**. Conversely, the BCC structure followed a PPR response, expanding laterally under compression; its PPR behavior was further validated by the FEM simulation results (Figure **S8**, Supporting Information). The SC structure, however, exhibited severe asymmetric bending, leading to structural instability rather than uniform deformation. The compressibility of the four structures was also analyzed using stress–strain measurements (Figure **2g**). The AMM and BCC structures exhibited similar behavior at low strains; however, the BCC structure underwent a sharp stress increase beyond 40% strain owing to densification effects from its diagonally interconnected struts. The SC structure initially resisted deformation but plateaued at 20%–30% strain, indicating a non-uniform load distribution that might contribute to structural instability. Among these structures, C-AMM exhibited the highest stress values. The increased mechanical resistance can be attributed to the presence of CNT coating, which reinforces the structure. Although this modification enhances electrical conductivity for sensing applications, it also reduces compressibility compared to uncoated AMM. Finally, Figure **2h** presents the strain-dependent Poisson's ratio of AMM, C-AMM, and BCC structures. The SC structure was excluded because its framework deformed asymmetrically under compression, preventing the reliable calculation of the Poisson's ratio. Initially, all structures exhibited PPR behavior, with values peaking in the vicinity of 0.4–0.5 at low strains. However, as the compressive strain increased, AMM and C-AMM entered the NPR regime, reaching their minimum Poisson's ratio at ≈10%–15% strain before gradually recovering at higher strains. This effect was more pronounced in AMM, which attained a lower minimum Poisson's ratio, indicating a stronger auxetic response. The CNT coating in C-AMM slightly reduced the magnitude of NPR owing to the increased stiffness restricting ligament rotation and buckling. Unlike these auxetic structures, the BCC structure maintained a PPR throughout compression, showing no transition to the NPR regime.

2.3 Capacitive and Resistive Sensing Enabled by AMM Structures

Leveraging the structural advantages of AMM, capacitive and resistive tactile sensors were fabricated to assess their electromechanical performance (see the Experimental Section and Figures **S9** and **S10**,Supporting Information for fabrication details). Each sensing mechanism exploits the deformation-driven characteristics of AMM—capacitive sensing responds to geometric changes in electrode spacing and dielectric properties, while resistive sensing detects pressure through contact modulation across CNT-coated conductive layers. **Figure 3a** presents the fabricated capacitive sensor, which incorporates an AMM core as the sensing layer between two Cu/Ecoflex electrodes. The sensing behavior was further analyzed through FEM simulation, as shown in Figure **3b**. The capacitance of the sensor is given by the parallel-plate capacitor model as $C = \varepsilon_{eff}A/d$, where A is the electrode area, and d is the electrode gap. In the initial state, the AMM maintains a defined electrode separation with air occupying the voids. Under compression, the electrode gap is reduced and internal air is displaced by the solid elastomeric material, increasing ε_{eff} of the dielectric layer. This dual effect—gap reduction and dielectric densification—synergistically contributes to the observed capacitance change, in accordance with the parallel-plate model.

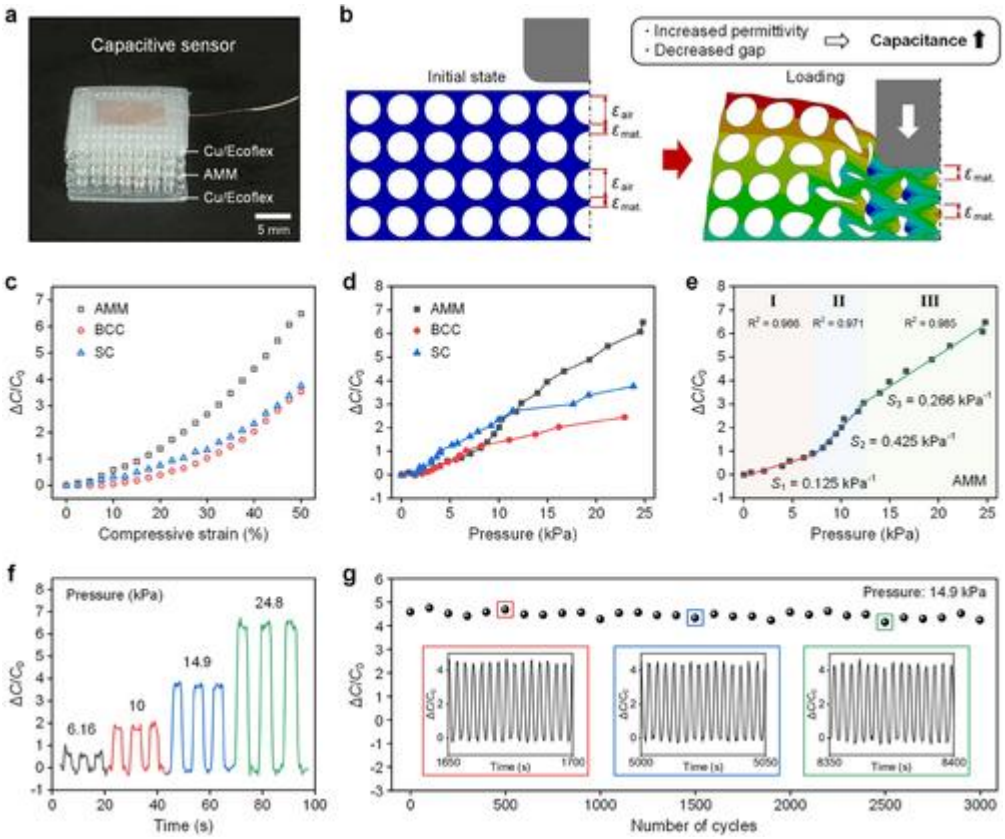

Figure 3

Open in figure viewerPowerPoint

Capacitive sensing performance of AMM-based tactile sensor. a) Photograph of fabricated capacitive sensor composed of an AMM sandwiched between Cu/Ecoflex electrodes. b) Schematic of sensing mechanism. Under compressive loading, both the decreased electrode gap and increased effective permittivity contribute to the capacitance increase. c) Relative capacitance change as a function of compressive strain for three different structures. d)

Pressure-dependent capacitive responses. Among the structures, the AMM-based sensor demonstrates the greatest increase in $\Delta C/C_0$, particularly at higher pressures. e) Piecewise linear fitting of AMM sensor response, divided into three regimes with corresponding sensitivities. f) Dynamic pressure response of AMM-based sensor under multiple pressure levels, confirming stepwise signal modulation. g) Long-term durability test over 3000 loading cycles at 14.9 kPa. The sensor maintains stable performance with minimal signal degradation. Insets: representative signal profiles at different time points.

To evaluate the electromechanical performance of the capacitive sensor, the relative capacitive change ($\Delta C/C_0$) was measured under compressive strain and applied pressure.
Figure **3c** presents the capacitive response of the sensors as a function of strain and applied pressure. Across all structures, the capacitance increases as compression reduces the electrode gap, enhancing charge storage. However, the AMM-based sensor exhibits a significantly steeper capacitance rise, particularly at higher strain levels, compared to the BCC and SC structures. Notably, AMM and BCC share the same initial porosity and show comparable stress-strain behavior under compressive loading (Figure **2g**), indicating similar overall deformability. Despite this, the AMM structure yields a greater capacitance change under identical strain. This contrast suggests that the enhancement arises not from global deformation, but from differences in how the internal dielectric region is reconfigured. The enhanced capacitance change in AMM originates from its auxetic behavior, which increases ε_{eff} of the sensing region. In our design, the dielectric layer consists only of elastomer and air; thus, the redistribution of material during compression directly affects ε_{eff}. In BCC and SC structures, compression leads to lateral expansion or asymmetric deformation, allowing dielectric material to move away from the central sensing region and limiting ε_{eff} growth. In contrast, AMM contracts inward owing to its NPR, forcing more dielectric material into the region between the electrodes. This inward collapse reduces the internal air volume and concentrates solid material where it most effectively contributes to dielectric enhancement, resulting in significantly greater ε_{eff} and amplified capacitance change. To compare the overall pressure-dependent response across different sensor architectures, $\Delta C/C_0$ was measured as a function of applied pressure (Figure **3d**). Among the three structures, the AMM-based sensor exhibited the largest capacitive change under increasing pressure. This enhanced response under identical pressure conditions reflects the greater compressibility of the AMM and its ability to concentrate the mechanical input into localized dielectric changes—an outcome consistent with the strain-stress-capacitance relationship depicted in Figures **2g** and **3c**.

To further analyze the pressure-response behavior of the AMM-based capacitive sensor, a piecewise linear fitting was applied to the $\Delta C/C_0$–pressure curve (Figure **3e**). The response is divided into three distinct regimes, each corresponding to a different stage of structural deformation. In the initial region (regime I, 0–7 kPa), the capacitance increases gradually, reflecting the elastic deformation of the AMM structure prior to the onset of auxetic behavior. This regime coincides with the early strain range in Figure **2h**, where the Poisson's ratio remains positive or near zero, and the deformation is primarily characterized by minor bending of ligaments. In the intermediate pressure range (Regime II, 7–12 kPa), the capacitance response exhibits the steepest slope. This rapid increase arises from the onset of buckling-driven inward contraction in the AMM framework, which significantly raises ε_{eff} of the dielectric layer. This

transition aligns with the strain range where the AMM demonstrates its most pronounced auxetic response, as indicated by the minimum Poisson's ratio in Figure **2h**. At higher pressures (regime III, 12–25 kPa), the capacitance continues to rise but with a reduced slope. This behavior is attributed to structural densification, which further limits ligament rotation and reduces the NPR effect. As the deformation saturates, the dielectric redistribution becomes less efficient, leading to a more moderate rate of capacitance increase. The corresponding sensitivities were calculated to be 0.125, 0.425, and 0.266 kPa^{-1} for regimes I, II, and III, respectively.

The dynamic performance of the AMM-based capacitive sensor was evaluated under various pressure conditions. As shown in Figure **3f**, the sensor produced distinct and repeatable capacitive responses when stepwise pressures between 6.16 and 24.8 kPa were applied. This confirmed its ability to differentiate multiple pressure levels with high fidelity. Furthermore, the response and recovery times were measured to be 156 and 104 ms, respectively, under a stepwise pressure input of 10.2 kPa (Figure **S11**, Supporting Information). The reversibility and hysteresis characteristics were examined by applying and subsequently removing pressure in a sequential manner (Figure **S12**, Supporting Information). The output closely matched the pressure profile in both loading and unloading phases, showing minimal hysteresis and strong repeatability. Long-term durability is a critical factor for the practical application of tactile sensors. To verify durability, the sensor underwent 3000 loading cycles at a constant pressure of 14.9 kPa (Figure **3g**). The output amplitude remained consistent throughout the test. The representative waveforms extracted from early, middle, and late cycles confirmed the mechanical robustness of the AMM structure and its ability to maintain stable signal characteristics over time. Additionally, the capacitance fully recovered after unloading, indicating negligible structural fatigue and complete mechanical restoration. In addition to mechanical durability, the thermal stability of the capacitive sensor was also examined (Figure **S13**, Supporting Information). The baseline capacitance remained nearly constant, with a maximum variation of only 0.053 over the temperature range of 25–60 °C, confirming stable operation under ambient thermal fluctuations.

In parallel with the capacitive configuration, a resistive-type tactile sensor was implemented using the same AMM architecture. To enable piezoresistive sensing, the AMM surface was coated with conductive CNTs, forming a pressure-responsive network. As shown in **Figure 4a**, the resulting C-AMM sensor is composed of a CNT-coated AMM core sandwiched between two CNT/Ecoflex composite electrodes, forming a through-thickness conduction pathway. The working principle is illustrated in Figure **4b**. Upon compression, the AMM exhibits inward contraction due to its NPR, which concentrates deformation toward the structural core and increases the proximity between CNT-coated ligaments. This facilitates the formation of additional micro-contact sites and shortens the inter-electrode distance, collectively enhancing conductivity under load. The piezoresistive behavior was evaluated by measuring the normalized current change ($\Delta I/I_0$) as a function of compressive strain and pressure. Three lattice configurations were compared: C-AMM, CNT-coated BCC (C-BCC), and CNT-coated SC (C-SC). As shown in Figure **4c**, all sensors showed increasing current with strain, but the C-AMM exhibited a sharply accelerated response beyond 30% strain. This enhancement is attributed to the NPR-induced contact densification. In contrast, BCC structures with a PPR expand laterally, which can reduce contact overlap and limit force localization. The SC structure undergoes asymmetric

bending, leading to localized strain concentration and irregular conductive path formation. These deformation characteristics result in reduced and less consistent sensing responses relative to the C-AMM. A similar trend appears in the pressure-dependent measurements (Figure **4d**), where the C-AMM sensor shows enhanced sensitivity, particularly beyond 15 kPa. The *I–V* characteristics further confirm pressure-dependent current increases while maintaining an ohmic response (Figure **S14**, Supporting Information). These results collectively highlight the geometric advantage of the auxetic AMM in improving contact dynamics and enhancing piezoresistive sensitivity under mechanical loading.

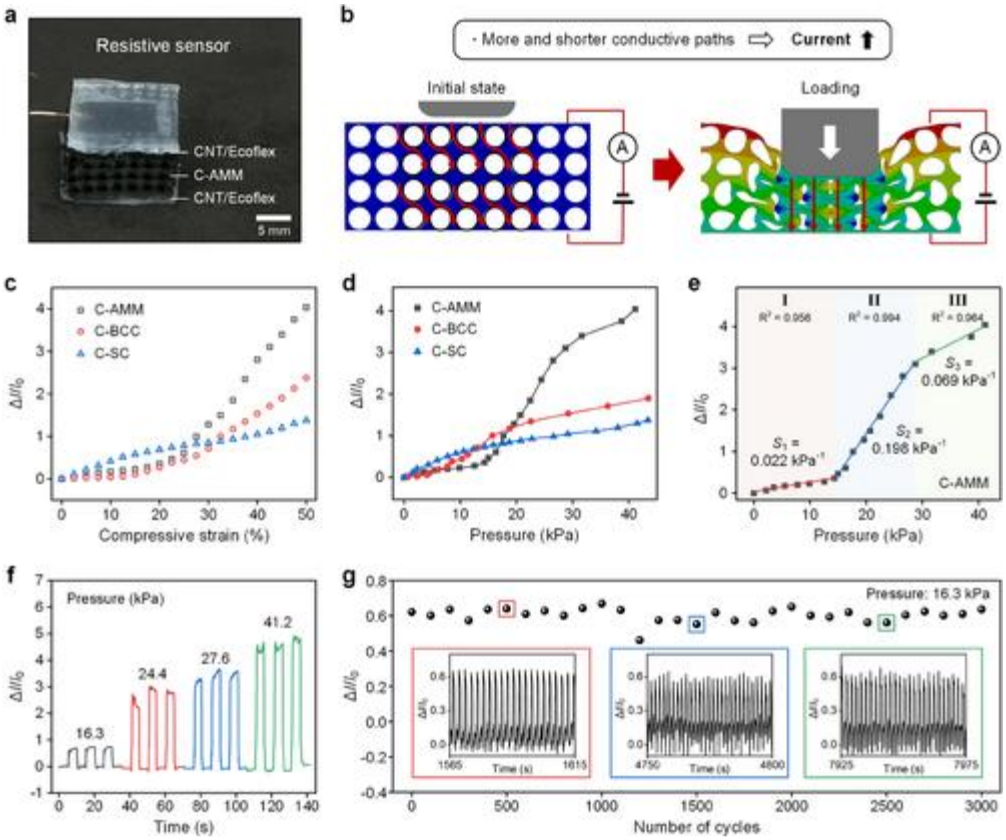

Figure 4

Open in figure viewerPowerPoint

Performance of C-AMM-based resistive tactile sensor. a) Photograph of fabricated resistive sensor, consisting of a C-AMM core between CNT/Ecoflex composite electrodes. b) Schematic of resistive sensing mechanism. Pressure-induced deformation brings CNT-coated ligaments into closer contact, forming more and shorter conductive pathways. c) Normalized current change versus compressive strain for three structures. d) Normalized current change under varying pressures. The C-AMM shows the largest signal change owing to auxetic-driven conductive network reconfiguration. e) Piecewise linear fitting of $\Delta I/I_0$ as a function of pressure, showing three sensitivity regimes. f) Stepwise pressure response of C-AMM sensor from 16.3 to 41.2 kPa. g) Cyclic durability test at 16.3 kPa over 3000 cycles, demonstrating signal repeatability and mechanical robustness.

The pressure-dependent response of the C-AMM resistive sensor was analyzed using piecewise linear fitting (Figure **4e**). The curve was divided into three regimes, corresponding to the different stages of structural deformation. Although similar in trend to the capacitive response (Figure **3e**), the piezoresistive sensitivity shows distinct values of 0.022, 0.198, and 0.069 kPa^{-1} for regimes I (0–14 kPa), II (14–29 kPa), and III (29–41 kPa), respectively. The steepest response in regime II reflects the active formation of conductive pathways driven by inward deformation, consistent with the onset of NPR behavior observed earlier in Figure **2h**. The performance stability of the C-AMM-based resistive sensor was validated through dynamic tests. As shown in Figure **4f**, the sensor produces distinct and repeatable responses under stepwise pressure inputs up to 41.2 kPa. In addition, the sensor exhibited response and recovery times of 151 and 152 ms, respectively, under a stepwise pressure input (10.2 kPa) (Figure **S15**, Supporting Information). The signal amplitude and waveform fidelity are consistently maintained throughout 3000 loading cycles at 16.3 kPa (Figure **4g**), confirming its mechanical durability and signal stability during prolonged operation. To further evaluate its environmental reliability, the resistive sensor was tested under varying temperature conditions (Figure **S16**, Supporting Information). The baseline current remained highly stable across 25–60 °C, with a maximum deviation of ≈0.013. This minor fluctuation is significantly smaller than the pressure-induced signal levels, indicating that sensor performance is largely unaffected by ambient thermal changes.

To comprehensively evaluate the performance of the AMM-based tactile sensors, we conducted a comparative analysis against recently reported 3D-printed tactile sensors (Table **S1**, Supporting Information). Key performance metrics, including sensitivity, sensing range, response/recovery times, and durability, were benchmarked across both capacitive and resistive configurations. In particular, when the trade-off between sensitivity and measurable pressure range is considered, our sensors are positioned among the higher-performing devices, as illustrated in the sensitivity-range plot (see Figure **S17**, Supporting Information for detailed discussion). It is important to note that the auxetic AMM architecture imparts substantially enhanced sensitivity compared to other porous geometries fabricated using the same base material. Because this enhancement is driven by structure rather than material composition, further improvements are anticipated when softer elastomers are employed. This structural adaptability strongly underscores the versatility and scalability of the proposed structure-centric approach for high-performance tactile sensing.

2.4 Practical Demonstration of AMM-Based Tactile Sensors

The functionality of the AMM-based tactile sensors was validated through two application-oriented demonstrations. First, a 4 × 4 resistive sensor array was developed to enable spatial pressure mapping and object classification. As shown in **Figure 5a**, the array consists of 16 C-AMM sensing units arranged in a grid, each integrated between patterned CNT/Ecoflex electrodes. Four electrodes are patterned on both the top and bottom surfaces, forming an addressable matrix configuration suitable for multiplexed signal acquisition (see Figures **S18** and **S19**, Supporting Information for the detailed device dimensions, multilayer configuration, and circuitry). To assess its spatial resolution and pressure discrimination

capability, the array was subjected to various input conditions, including non-contact, light touch, single-point low pressure, and multi-point high pressure (Figure **5b**). The output reliably captured both contact position and pressure magnitude, confirming accurate spatial mapping and independent signal generation from each pixel (Figure **S20** and Movie **S2**, Supporting Information). For object classification, the array was used to identify four representative items—a tennis ball, a baseball, an orange, and an apple—selected for their distinct size and weight (Figure **5c**). When placed on the array, each object produced a unique pressure distribution pattern based on its geometry and load. These patterns were preprocessed and analyzed using a *k*-nearest neighbors (*k*-NN) algorithm. The classification results are shown in Figure **5d**, wherein the identified object label is displayed in real-time on a monitor (Movie **S3**, Supporting Information). The array consistently distinguished the four objects regardless of their contact position or orientation. This position-independent classification capability demonstrates the robustness of the AMM-based sensor array, which accurately interprets spatial pressure patterns without requiring precise alignment. Such flexibility is essential for practical tactile interfaces, wherein uncontrolled object placement is common.

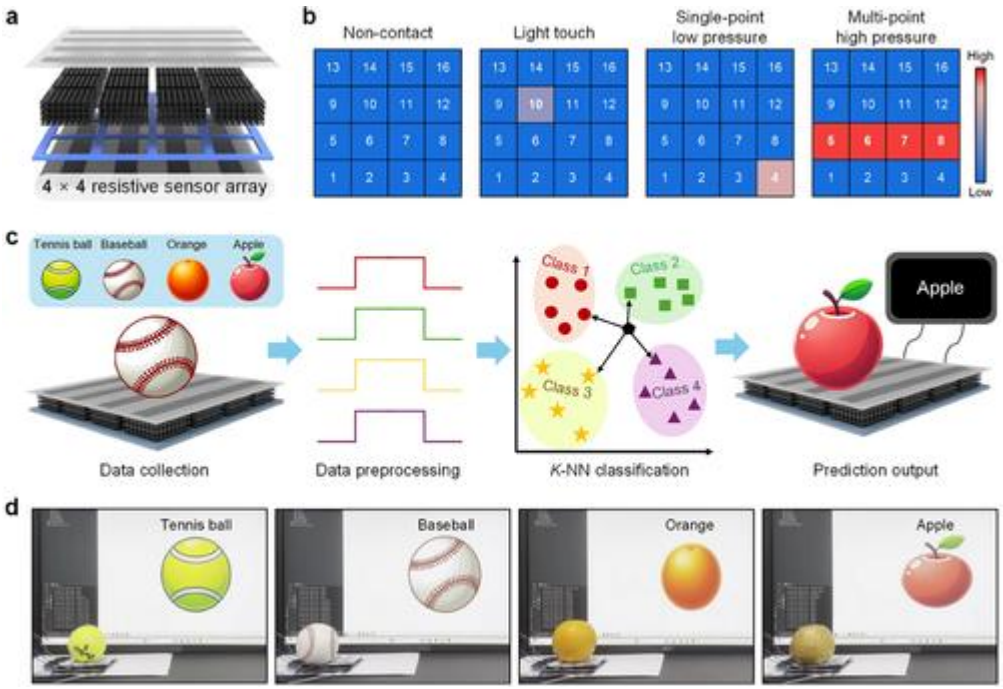

Figure 5

Open in figure viewerPowerPoint

Spatial pressure mapping and object classification using a C-AMM-based resistive sensor array. a) Exploded schematic of resistive sensor array composed of 16 C-AMM units embedded between patterned CNT/Ecoflex electrodes. b) Pressure mapping results under four representative conditions: non-contact, light touch, single-point low pressure, and multi-point high pressure. c) Schematic of object classification process using the sensor array and *k*-NN algorithm. Four distinct objects—a tennis ball, a baseball, an orange, and an apple—generate unique pressure patterns based on size and weight. d) Photographs of real-time object classification results are displayed on a monitor upon placement of each object.

Among potential applications, wearable tactile systems are highly suitable for implementing the proposed AMM-based sensors. In these environments, embedded tactile sensors are often subject to complex mechanical constraints, including confinement within rigid housings. Conventional lattice structures based on PPR typically deform through lateral expansion when compressed (**Figure 6a**). However, when these structures are embedded, such lateral deformation is mechanically restricted, resulting in diminished compressibility and degraded sensing performance. In contrast, auxetic AMMs deform inward under pressure due to their NPR, allowing localized strain concentration in the sensing region without relying on lateral displacement. To validate this structural advantage in confined settings, we performed a comparative set of experiments under embedded and freestanding conditions. Resistive tactile sensors were prepared using three distinct lattice designs: C-AMM, C-BCC, and C-SC. Each sensor was tested both in an unconstrained (freestanding) state and while embedded in a rigid frame that restricted lateral deformation, simulating structural confinement typical of wearable systems (Figure **S21**, Supporting Information). As shown in Figure **6b**, all three sensors exhibited similar mechanical responses under low strain, indicating negligible influence of embedding in the early deformation regime. However, as compressive strain increased, both the BCC- and SC-based sensors showed a marked increase in stress relative to their freestanding counterparts. This behavior indicates a stiffening effect due to suppressed lateral expansion. In contrast, the AMM-based sensor retained a comparable stress–strain profile under both freestanding and embedded conditions, owing to its geometry-induced inward deformation mechanism. These mechanical trends were further reflected in the electrical performance. As shown in Figure **6c**, the normalized current responses under applied pressures of 10 and 20 kPa were significantly reduced for the BCC- and SC-based sensors when embedded, confirming reduced effective deformation. In contrast, the AMM-based sensor maintained consistent signal responses across both test conditions. These results demonstrate that the auxetic AMM structure offers enhanced robustness and pressure sensitivity even in mechanically constrained environments, underscoring its utility for embedded tactile sensing applications such as smart insoles.

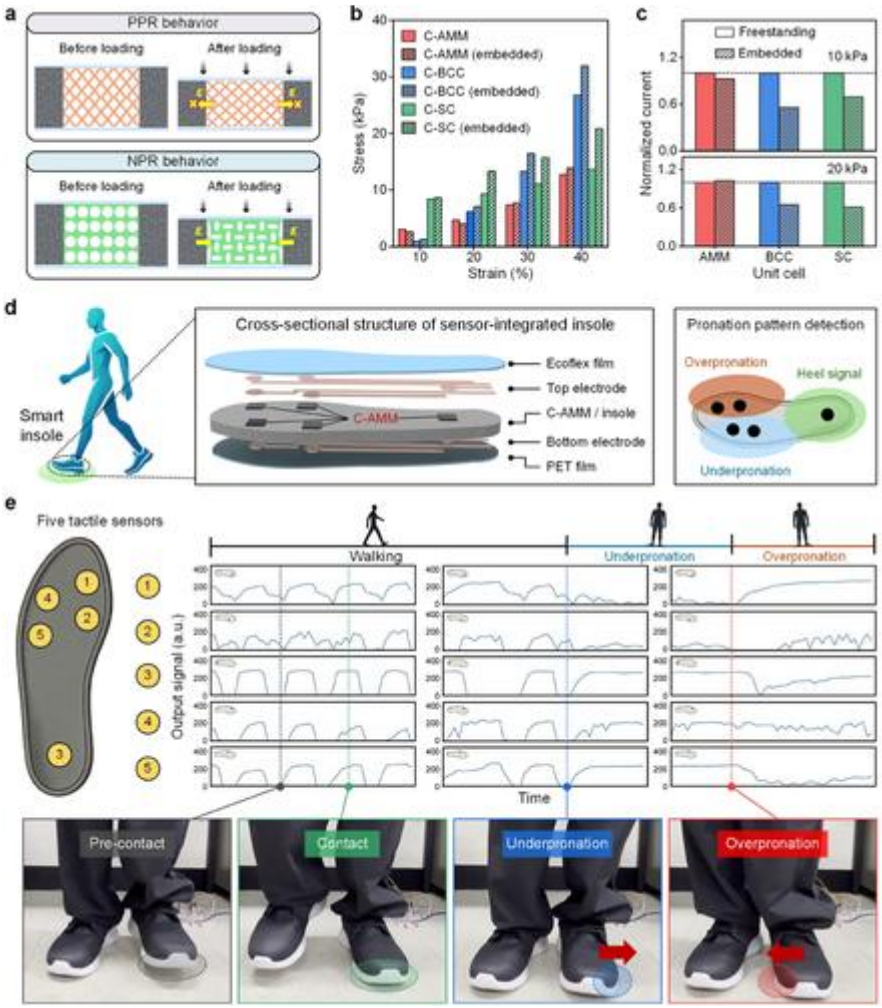

Figure 6

Open in figure viewerPowerPoint

Smart insole demonstration for gait monitoring and pronation analysis. a) Comparison of pressure response between conventional PPR and auxetic NPR structures. The NPR behavior of AMM promotes inward contraction, enabling effective sensing even when lateral deformation is constrained within the insole. b) Stress–strain relationship of resistive tactile sensors based on AMM, BCC, and SC structures under freestanding and embedded conditions. c) Normalized current responses of each sensor at 10 and 20 kPa under freestanding and embedded conditions. The AMM-based sensor preserves a consistent signal output, while the BCC- and SC-based sensors exhibit performance degradation when embedded. d) Conceptual illustration of wearable insole system embedded with five AMM-based tactile sensors. e) Real-time sensor outputs during walking, underpronation, and overpronation, with corresponding foot posture images. Lateral sensors (3–5) respond more in underpronation, while medial sensors (1–3) are dominant in overpronation.

To explore its applicability in wearable systems, the AMM-based tactile sensor was integrated into a smart insole platform for gait monitoring and pronation analysis (Figure **6d**). Five C-AMM sensors were strategically embedded at key plantar locations within a multilayered insole composed of Ecoflex, polyethylene terephthalate (PET), and copper electrodes

(Figures **S22** and **S23**, Supporting Information). Figure **6e** presents real-time gait monitoring results obtained using the sensor-integrated insole (Movie **S4**, Supporting Information). During normal walking, the sensors exhibited a sequential activation corresponding to heel and forefoot contact. In underpronation, the lateral sensors (3, 4, and 5) showed heightened responses, reflecting outward foot loading. Conversely, in overpronation, increased signals were observed from the medial sensors (1, 2, and 3), corresponding to inward rolling during stance. These distinct spatial profiles enable the reliable detection of gait deviations, demonstrating the effectiveness of the proposed system for wearable biomechanical assessment. Since insoles are frequently subjected to bending during gait, especially on uneven surfaces, it is important to verify that the sensor output is minimally influenced by such deformation. To further assess the output signal under bending deformation, the insole-integrated sensor array was tested on curved surfaces with different radii (Figure **S24**, Supporting Information). While the output signal slightly increased with curvature, it remained significantly lower than the response to vertical pressure during standing, confirming that the sensor primarily responds to normal loading.

3 Conclusion

We developed a 3D-printed tactile sensing platform based on a mechanically engineered AMM framework. Utilizing DLP additive manufacturing, we realized a geometrically simple yet functionally versatile AMM design, consisting of a cubic lattice with a central spherical void. This structure exhibited an NPR behavior under compression, enabling inward deformation that localized strain and enhanced sensing performance. By integrating this architecture into both capacitive and resistive sensing configurations, we demonstrated that the AMM structure offers a material-agnostic, structure-centric approach for tactile sensing. The capacitive sensor leveraged pressure-induced changes in both electrode spacing and effective permittivity, while the resistive sensor exploited the formation of conductive pathways in CNT-coated AMM ligaments. Both configurations exhibited superior pressure sensitivity compared to conventional PPR porous structures fabricated from the same material system. The mechanical behavior of the AMM, including compressibility and auxeticity, was systematically analyzed through FEM simulations and experimental tests, with porosity-controlled variations confirming the role of architectural tuning. In both capacitive and resistive modes, the sensors exhibited distinct, repeatable pressure-dependent responses and long-term stability under cyclic loading. The practical applicability of the AMM-based sensors was validated through two demonstrations: 1) a 4 × 4 sensor array capable of pressure mapping and object classification via machine learning, and 2) a smart insole system for gait monitoring and pronation analysis. The obtained results underscore the robustness, scalability, and flexibility of the proposed AMM-based platform in real-world scenarios. The structure-centric design approach, decoupled from specific material choices, offers a universal strategy for building next-generation tactile sensors across diverse modalities and form factors. Furthermore, the demonstrated ability to maintain stable sensing performance under embedded and mechanically confined conditions highlights the practical value of the AMM design. Beyond the current demonstrations, potential application domains include robotic end-effectors with integrated tactile feedback, smart orthotic systems, and intelligent mats or beds for posture monitoring and sleep analysis.

4 Experimental Section

Fabrication of AMM and Other Lattice Structures

The AMM structures, along with body- BCC and SC lattices used for control experiments, were fabricated using a DLP-based 3D printer (IMD, Carima). A photo-curable polyurethane resin (CUKE05C, Carima) was employed as the printing material for all structures to ensure consistent mechanical properties. This semitransparent resin was optimized for UV curing at 405 nm, and exhibits a viscosity of 1050 cps, a cured tensile strength of 2.2 MPa, and an elongation at break of 220%. The printer was equipped with a high-definition DMD featuring a resolution of 1920 × 1080 pixels, corresponding to an in-plane resolution of 50 μm × 50 μm. Each layer was exposed to UV light at an energy density of 9.65 mW cm^{-2} for 4.4 s, and the layer thickness was maintained at 50 μm to achieve high structural fidelity. After printing, the specimens were immersed in 99.5% isopropyl alcohol and cleaned in an ultrasonic bath (SD-250H, Mujigae) to remove the residual uncured resin.

Mechanical and Structural Characterization

Optical images of the printed lattice structures were obtained using an optical microscope (AM-413T, Dino-Lite) to assess macrostructural morphology and printing fidelity. High-resolution imaging of the microscale architecture was performed via field-emission SEM (IT-800SHL, JEOL). To visualize deformation behavior under compressive loading, in situ SEM imaging was conducted using a tensile and compression stage (MT200, Deben) integrated within a variable-pressure SEM system (AIS2500C, Seron Tech). FEA was carried out using engineering simulation software (ANSYS Workbench, ANSYS) to simulate the deformation behavior of the lattice structures under compressive loading. A custom-built universal testing system equipped with a force gauge (DTG-1000N, DigiTech) was used to apply vertical loading while simultaneously measuring the applied force. The corresponding pressure was calculated by dividing the measured force by the effective contact area between the sample and the compression plate.

Fabrication of Capacitive and Resistive Tactile Sensors

Capacitive and piezoresistive tactile sensors were fabricated using an AMM framework and packaged with flexible electrode layers composed of silicone rubber (Ecoflex 0030, Smooth-On). The Ecoflex was mixed with its curing agent in a 1:1 weight ratio, poured into polylactic acid (PLA) molds fabricated via fused deposition modeling, and cured at room temperature for 4 h to produce 500 μm-thick films. The cured films were coated with silicone adhesive (Sil-Poxy, Smooth-On) and laminated onto both the top and bottom surfaces of the printed structures. The adhesive layer was allowed to cure at room temperature for 10 min to ensure mechanical stability. For the capacitive configuration, double-sided conductive copper tape was used as the electrode. These electrodes were sandwiched between the AMM core and Ecoflex films during packaging, allowing capacitance to be measured across the vertical axis of the structure. Copper tape was selected for its high conductivity and smooth surface finish, which facilitated reliable detection of capacitance changes under low-noise conditions. The piezoresistive

sensors utilized C-AMM cores and CNT membrane electrodes patterned onto the Ecoflex substrates. To fabricate the electrodes, a PET masking film was prepared using a precision cutter (Cameo 4 Pro, Silhouette) to define 8 mm × 8 mm square openings. The masking film was affixed to the Ecoflex substrate, and a 0.1 wt.% dispersion of multi-walled carbon nanotubes (MR99, Carbon Nano-material Technology) in chloroform was spray-coated through the mask using a spray coater (BBT-DFP001, Beetle Bug) at a spraying distance of 20–30 cm. The CNT solution was homogenized prior to coating using an ultrasonic homogenizer (HD 4100, Bandelin). After the removal of the mask, patterned CNT electrodes were formed on the film. The AMM core was dip-coated in the same CNT dispersion for 10 min to form a conformal conductive network, then dried on a hot plate at 40 °C for 6 h to remove residual solvent. The coated structure was assembled between CNT-coated Ecoflex layers using silicone adhesive to complete sensor packaging.

Electromechanical Testing of Tactile Sensors

The capacitive and piezoresistive responses of the fabricated tactile sensors were characterized under controlled compressive loading conditions. All measurements were performed using the same custom-built universal testing system. For capacitive sensing, the change in capacitance was monitored using a precision LCR meter (4100, Wayne Kerr) under stepwise and cyclic loading. The capacitance data were acquired at a fixed frequency and voltage level to evaluate pressure-dependent characteristics and sensitivity. For piezoresistive measurements, the current-voltage characteristics and pressure-induced current variation were recorded using a sourcemeter (2636B, Keithley). Temperature-dependent experiments were conducted by placing each sensor on a temperature-controlled hot plate (HS-20, LK Lab Korea).

Application Demonstrations Using a Sensor Array and Smart Insole System

For the array demonstration, 16 C-AMM sensors were placed into a PLA mesh frame fabricated via fused deposition modeling. A silicone rubber film (Ecoflex 0030, Smooth-On) was cast using a reverse mold, and CNT electrodes were patterned onto the film by spray coating a 0.1 wt.% MWCNT solution through a PET-based masking film. Four CNT electrodes were formed on each side in an orthogonal arrangement to configure the matrix. Copper wires were attached to the electrodes using silver paste for electrical connection, and the array was interfaced with a microcontroller unit (Arduino Uno) for signal acquisition and real-time visualization. For the smart insole system, five cutouts were created in a commercial insole to accommodate the sensors. Copper tape was patterned on silicone rubber and PET films to form the top and bottom electrodes, respectively. The C-AMM sensors were inserted into the cutouts and packaged between the two films using Scotch tape (3 M). The system was connected to an Arduino Uno, and pressure responses were visualized through a custom Python-based interface. Informed consent was obtained from all participants prior to the experiments. Ethical approval was not required for this study under institutional guidelines, as no invasive procedures or identifiable personal data were involved.